

A COMBINED WAVENUMBER-FREQUENCY AND TIME EXTENDED EOF
APPROACH FOR TRACKING THE PROGRESS OF MODES OF LARGE-SCALE
ORGANIZED TROPICAL CONVECTION

Paul E. Roundy and Carl J. Schreck III

University at Albany

State University of New York

Submitted to The Quarterly Journal of the Royal Meteorological Society July 2008

Corresponding Author Address:

Paul E. Roundy
University at Albany
Department of Atmospheric and Environmental Sciences
DEAS-ES 351
Albany, NY 12222

Abstract

An algorithm combining filtering in the wavenumber frequency domain with time extended empirical orthogonal function (EEOF) analysis is developed and applied to diagnose and track signals associated with modes of organized moist deep convection in the tropics. The wavenumber-frequency spectrum of outgoing longwave radiation (OLR) is broken down into 5 broad filter bands in order to concentrate signals associated with the Madden Julian Oscillation, convectively coupled equatorial Rossby, Kelvin, and Mixed Rossby gravity waves, easterly waves, and low frequency variations such as the El Niño/Southern Oscillation (ENSO). The EEOF patterns are obtained from analysis of the filtered data, and principal component (PC) time series are generated by projection of temporally smoothed, but otherwise unfiltered data onto the EEOF patterns. Filtered data are reconstructed by taking the product of the EEOF patterns and the corresponding PCs. These reconstructed data compare well with unfiltered OLR anomalies and with OLR anomalies filtered in the wavenumber frequency domain for the same modes. The method is easily applied in real time without the distortion at the end of the dataset observed in data filtered in the wavenumber frequency domain.

Key words: Madden Julian Oscillation, El Niño/Southern Oscillation, convectively coupled equatorial waves

(1) Introduction

(1.1) Background

Although most numerical models do not adequately represent the evolution of organized moist deep convection in the tropics (e.g., Lin et al. 2006), analyses of observations suggest that some modes of organized convection evolve systematically in time and space. Such systematic evolution may be exploited in statistical forecast models if a basis of time indices for the modes can be obtained. Numerous weather and climate modes evolve with synoptic to planetary scale anomalies of moist deep convection in the tropics, including but not limited to the Madden Julian Oscillation (MJO, Madden and Julian 1994; Zhang 2005), synoptic to planetary scale waves (e.g., Kiladis et al. 2008), and climate processes such as the El Niño/Southern Oscillation (ENSO), the Indian Ocean dipole, and the Atlantic meridional mode. This work presents a new approach for extracting signals of some of these modes of organized convection for the purpose of real time diagnostics and forecasting, by combining filtering in the wavenumber frequency domain (Wheeler and Kiladis 1999; Roundy and Frank 2004a) with time extended empirical orthogonal function (EEOF) analysis. The extracted signals may then be applied to track the different modes in real time and to predict variations in the weather associated with these modes through statistical models.

Numerous theoretical, observational, and modeling studies motivate further work in analyzing intraseasonal oscillations and waves in the tropical atmosphere for real time weather prediction. Many authors have attempted to reduce the apparent chaos of tropical weather by drawing analogs to a set of propagating wave modes derived from

models of shallow-water on the equatorial beta plane (a review of these waves is given by Kiladis et al. 2008). Matsuno (1966) and Lindzen (1967) analyzed these simple linear models and revealed a family of waves that propagate parallel to the equator. The waves form patterns that are either symmetric or antisymmetric across the equator, and they include Rossby, Kelvin, mixed Rossby gravity, and inertio gravity waves. A principal set of these waves have become known as “convectively coupled equatorial waves” because of their relationships with moist deep convection (e.g., Wheeler and Kiladis 1999; Wheeler et al. 2000; Yang et al. 2003, 2007a,b,c, and many others). The structures of the observed waves vary from the theoretical patterns in response to differences in background wind and convective states (e.g., Lindzen 1971, 2003; Majda et al. 2004; Wang and Xie 1996; and many others).

In addition to these modes having theoretical analogs, observational analyses have revealed the MJO and African easterly waves without obvious counterparts in the shallow water theory. The MJO is directly associated with more variance in global convection than any other tropical mode observed in the 2-100 day band. The synoptic scale “easterly waves” propagate westward from Africa across the Atlantic and East Pacific during Boreal summer and fall (e.g., Carlson 1969; Reed et al. 1977; Kiladis et al. 2006), and are occasionally associated with formation of tropical cyclones.

The advent of satellite based observations and reanalysis datasets greatly improved the analysis of these synoptic to planetary scale waves and their impacts (e.g., Yanai and Murakami 1970; Wallace and Chang 1972; Gruber 1974; Zangvil 1975; Zangvil and Yanai 1980; Zangvil and Yanai 1981; Liebmann and Hendon 1990; Hendon and Liebmann 1991; Takayabu 1994; and many others). Wheeler and Kiladis (1999)

analyzed outgoing longwave radiation (OLR) and temperature data in the zonal wavenumber frequency domain. Their results show how the MJO, easterly waves, equatorial modes, and tropical cyclones fit together in a broad spectrum of variability of clouds and dynamical fields. They found certain patterns in the wavenumber-frequency spectrum of OLR to be consistent with the predictions of wave dispersion from equatorial beta plane shallow water theory. This finding is astonishing because of the complexity of the earth-atmosphere system, which includes variable background winds and moist deep convection that would modify wave structure and propagation characteristics. By filtering OLR data for peak regions of the wavenumber-frequency spectrum that they linked to specific types of waves, extracting time indices for the waves from filtered data at specific geographical locations, and regressing data fields against these indices, Wheeler et al. (2000) further showed that convectively coupled waves have structures strikingly similar to those predicted by shallow water theory. Since the work of Wheeler and Kiladis (1999), study of waves in the equatorial region has moved from a largely academic problem considered by many to be of little relevance to day-to-day weather to a problem deeply relevant to forecasters and stakeholders around the world. As shallow water theory suggests, the observed waves evolve systematically, and systematic evolution might imply that signals of the different modes can be used in concert in statistical models to develop skillful predictions of the evolution of the weather.

In spite of progress in applying equatorial wave thinking to weather analysis and forecasting, operational forecast centers could still capitalize better on these potentially very useful results from the research community. Although climatologists and oceanographers have long recognized the potential importance of equatorial waves in the

ocean to the development and demise of El Niño (e.g., Battisti 1988), forecasters have only recently begun to recognize the relevance of atmospheric equatorial waves and related oscillations to weather analysis and prediction. The research community recognizes these waves to be among the principal building blocks of tropical weather and climate. The waves may also significantly influence weather prediction in the mid-latitudes because they modulate the development of tropical cyclones (e.g., Bessafi and Wheeler 2006; Frank and Roundy 2006) and because they help determine the geographical distribution of moist deep convection in the tropics that then modulates the development planetary scale overturning circulations and of planetary waves propagating into the midlatitudes (e.g., Weickmann et al. 1985, 1997, and others).

(1.2) Diagnosis and Tracking of Equatorial Waves and Intraseasonal Oscillations

Numerous authors have recently developed methods for diagnosing the progress of equatorial waves and the MJO. These methods can be loosely grouped into two general forms. These forms are temporal or spatial-temporal (zonal wavenumber-frequency) filtering (e.g., Wheeler and Kiladis 1999; Wheeler and Weickmann 2001; Roundy and Frank 2004) and projection of observed data onto empirically or theoretically defined spatial patterns associated with the different modes (e.g., Yang et al. 2003, 2007a,b,c; Wheeler and Hendon 2004). Each of these methods has been successful in specific applications, but only a subset is applicable in real time. Caveats must be considered when applying any of the techniques appropriate for real time.

(1.2.1) Fourier Filtering

Fourier filtering is applied to isolate signals associated with specific broad peaks in the wavenumber frequency domain that lie along the dispersion curves of equatorial

beta plane shallow water theory or that have otherwise been associated with known observed modes (e.g., Wheeler and Kiladis 1999; Roundy and Frank 2004a; and many others). Although effective in these applications, Fourier filtering distorts filtered data near the ends of datasets, complicating its application to analysis in real time (although Wheeler and Weickmann 2001 take advantage of the smearing effects of filtering to generate predictions of wave behavior). Many authors construct filters to enclose small regions of the wavenumber frequency domain immediately about the spectral peaks of interest. Such small Fourier filters would omit important spatial or temporal harmonics relevant to a process if the signal associated with that process is not sinusoidal, but would have the advantage of reducing the contributions of the red noise background (e.g., Wheeler and Kiladis 1999; Roundy et al. 2008). Nonlinear interactions between modes might increase or decrease the amplitudes of unfiltered anomalies associated with combinations of multiple modes, leading to misrepresentation of the amplitudes of waves apparent in data filtered for specific wave types.

(1.2.2) Projection Approaches

Projection of observed anomalies onto spatial patterns obtained from shallow water theory and empirical orthogonal function (EOF) techniques (Kim and Wu 1998) including the EOF (e.g., Wheeler and Hendon 2004), Hilbert EOF (also called the complex EOF), time extended EOF (EEOF), and singular value decomposition (SVD, e.g., Zhang and Hendon 1997; Weare 2003) have each been applied to dissect data to provide information about individual types of waves and intraseasonal oscillations. Yang et al. (2003, 2007a,b,c) projected observed data onto the patterns of waves obtained from shallow water theory, yielding substantial information associating observed wave patterns

with theoretical ones. Their results have contributed greatly to our understandings of the portions of observed waves that are characterized by wind patterns that are strictly consistent with the theoretical waves. However, observed waves corresponding to the theoretical ones may exhibit substantial patterns that are not constrained by pure symmetric or antisymmetric cross-equatorial symmetry in the wind field. Such asymmetric patterns would not project onto the idealized structures and would be lost in the projection process. The distorted patterns would influence the impacts of the waves on sensible weather, so they should not be ignored in operational analyses. Further, many propagating patterns of organized convection observed in the tropics do not correspond well with the shallow-water modes, so this projection approach cannot yield a comprehensive basis for propagating patterns of large-scale organized convection. In addition, the method would not be easily applied in real time because filtering in the wavenumber frequency domain for eastward- and westward-moving patterns is applied prior to taking the projections, and this filtering would lead to distortion near the end of the dataset.

Empirical projection approaches do not assume a priori the spatial structures of modes. EOF (or principal component) analysis is probably applied more frequently than other empirical approaches to analysis of the spatial patterns of atmospheric modes in real time. In the present context, an EOF is an eigenvector of the covariance matrix of a vector space in which individual members are time series of data at individual grid points minus the local time mean or the mean and the seasonal cycle. Each EOF mode represents a spatial pattern of temporal covariances in the data. Projection of the data onto a given EOF produces a principal component (PC) time series that reveals how

amplitude projecting onto the spatial pattern varies with time. The set of EOFs are orthogonal to each other, and the PCs form a basis for all of the temporal signals in the data from which they are extracted. Subsets of the EOFs are sometimes associated with particular modes of the physical system. One pair of eigenmodes describes the core structure of a propagating mode, and additional higher EOFs can be correlated with members of the leading pair part of the time and anticorrelated another part of the time (resulting in zero correlation across the length of the time series). These related higher modes can describe how the process changes in response to lower-frequency variations (e.g., higher EOFs associated with the MJO in equatorial zonal wind describe its relationship with ENSO, Kessler 2001). Groups of such higher modes might sometimes explain more variance in the process of interest than its core eigenmodes, such that the core modes may not be sufficient to describe the evolution of the process. Further, structures associated with a set of distinct physical modes are not necessarily orthogonal to each other, such that multiple processes may project onto the same EOF (e.g., the convective structures associated with ENSO, the MJO, equatorial Rossby waves, and convectively coupled Kelvin waves are not orthogonal in space, Roundy et al. 2008). Nevertheless, these methods have increased in popularity in recent years, in part because pairs of eigenmodes offer the convenience of a “phase space” approach to tracking propagating processes and tabling the relationships between those processes and other events (e.g., Wheeler and Hendon 2004).

EOF analysis is frequently applied to reduce noise in a dataset, since eigenmodes associated with noisy processes each tend to explain little variance when compared with the leading eigenmodes. Further, the PCs of a subset of eigenmodes associated with a

given weather process can be applied as spatially independent predictors of that process in regression models for diagnoses of the present state of the process and for prediction. Unlike Fourier methods, EOF analysis can be applied easily in real time without the risk of distortion at the end of a dataset.

(1.2.3) New Combined Filtering and EOF Approach

The purpose of this work is to introduce a combined wavenumber-frequency filtering and EEOF approach for diagnosing wave and climate variations from OLR data in a manner applicable in real time. Filtering is applied to focus the analysis on patterns associated with specific regions of the wavenumber-frequency domain. The EEOF analysis is then applied to the filtered data to determine the spatial-temporal structures associated with disturbances characterized by that part of the spectrum. The technique then provides ‘filtered’ data by projecting temporally smoothed but otherwise unfiltered data onto the patterns of the EEOFs. The method can be applied in real time without the distortion frequently observed at the ends of datasets associated with Fourier methods. The method is applied to extract the signals of different wave modes from unfiltered OLR anomalies for tracking the anomalies in real time or to derive time indices for the different modes that can be applied as predictors in linear regression forecast models for various weather events around the globe.

(2) Data and Methods

(2.1) Data

Interpolated OLR data, (Liebmann and Smith 1996) were obtained from the NOAA Earth System Research Laboratory (ESRL, formerly Climate Diagnostics Center) website. OLR is a relatively good proxy for moist deep convection in the tropics. This

analysis includes the period June 1, 1974 through December 2006. It is important to point out that different satellite platforms were used to obtain these data over the years. Equatorial crossing times varied between satellites and over time for individual satellites because of orbital decay, thus examination of long-term trends in these data is difficult. Some signals in the data characterized by interannual frequencies may therefore be associated with unnatural signals related to changes in the satellites. However, structures associated with the temporal evolution of observed intraseasonal convective events are not likely to be significantly influenced by these irregularities, and processes such as ENSO may be distinguished from the artificial signals. Although NOAA interpolated OLR data are not available in real time, NOAA uninterpolated OLR data are available and are interpolated at the time of processing. Here, interpolation is applied for a missing datum by averaging all available data within 5 degrees of latitude and longitude of the missing point and substituting the result for the missing datum.

(2.2) Extraction of EEOF Indices

Several steps are applied here in succession to extract wave and climate signals from the OLR data.

1. Filter the data for a selected band in the zonal wavenumber frequency domain.
2. Construct a matrix of time series of the data on a reduced grid.
3. Extend the matrix by padding it with the same data at time lags from the original data.
4. Calculate the leading EOFs of the extended matrix.
5. Reconstruct the matrix in 3 by using temporally smoothed but otherwise unfiltered data.

6. Generate indices of the wave and climate modes by projecting the data in 5 onto the eigenmodes of the filtered data found in 4.

Each of these steps is described in detail below.

(2.2.1) Wavenumber Frequency Filtering

Interpolated OLR data are processed by filtering for broad bands in the wavenumber-frequency domain. The wavenumber-frequency filters are applied by first performing the Fourier transform in longitude, followed by another transform in time (e.g., Wheeler and Kiladis 1999; Roundy and Frank 2004a). Fourier coefficients outside of the range of the filter are then set to zero and the filtered data are obtained by performing the inverse transform. The filters are shown plotted on a normalized OLR spectrum in Fig. 1. This spectrum was calculated as described by Wheeler and Kiladis (1999) except that cross-equatorial symmetry was not considered and the background was calculated by smoothing the total power 30 times with a 1-2-1 filter in both wavenumber and frequency.

Filters can be shaped and sized to isolate wave and climate signals in many different ways. Wheeler and Kiladis (1999) aligned their filters with dispersion curves obtained from shallow-water theory for equatorial waves (thus maintaining a logical connection to linear theory). Roundy (2008) and others have applied rectangular filters that enclose broader regions of the spectrum than are included in the filters of Wheeler and Kiladis (1999). Broad rectangular filters are applied here because data filtered for broad bands were not found to be sensitive to small changes in the domain of the filters. The smaller the filter, the larger the changes associated with variations in the filter size and shape. Broader filters also improve the resolution of waves that change propagation

characteristics as they move through different environments. The need for broader filters applies especially to ER waves, since slow-moving Rossby waves are distorted substantially by background wind patterns (e.g., Kiladis et al. 2008) and the dispersion curves modified by advection would not align well with those in a motionless background state. The broader filters applied here allow the algorithm to include more of the variance in the total OLR anomaly, thus increasing amount of the total variance that can be explained by the OLR modes derived by the method. Such broad filters would include more wave signal than would narrow filters, but this extra signal would come at the expense of additional noise from the spectral background (e.g., Wheeler and Kiladis 1999). This additional noise is then largely excluded by utilizing only the leading eigenmodes in the step 6.

Four wavenumber-frequency bands were applied in this analysis (as indicated in Figure 1). A fifth filtered dataset is constructed by applying a 100-day low pass filter to the OLR anomalies. Climate variations including ENSO and the Indian Ocean dipole dominate this dataset. Long-term trends and artificial variations such as different satellite crossing times might also appear.

(2.2.2) Reduce the Grid

Data from 25°N to 25°S are included in the EEOF computation. Computer memory constraints required that the global grid be reduced before the EEOF analysis by taking a subset of grid points. Data were first smoothed by a 12.5°-centered moving average in the zonal direction, then every third grid point was retained along each parallel. This smoothing dramatically diminishes signals associated with patterns higher than

wavenumber 10. The resolution in latitude was 2.5° equatorward of 15° latitude and 5° poleward of 15° . Future versions may allow higher spatial resolution.

(2.2.3) Extend the Data Matrix By Including the Same Data at Time Lags

Extended EOFs were generated for each filtered dataset by arranging timeseries of filtered data at each retained grid point into a matrix, then padding the matrix with the same data at time lags from the original dataset. Thirteen time-lagged datasets were included in each matrix. Thirteen was the upper limit due to computer memory limitations. The time lag between the different datasets is shorter for the lower time lags and longer for the higher lags, as shown in Table I. Note that the differences in lag length are also longer for lower frequency modes and shorter for higher frequency modes. The shortest time steps must be less than half of the shortest period intended to be resolved, and the longest lag should be close to the highest frequency included in the filter, or in the case of low-pass filtered data, it must be sufficiently long to resolve patterns relevant to real time analysis.

(2.2.4) Calculate the EEOF Patterns

EEOF patterns are the eigenvectors \mathbf{e} of the matrix $\mathbf{X}^T\mathbf{X}$, where \mathbf{X} is the extended matrix of filtered data, and T represents the matrix transpose.

(2.2.5) Generate a New Data Matrix From Unfiltered Anomalies

Steps 5-6 may be applied at any time throughout the period of the predictor set, including in real time. A new data matrix of temporally smoothed but otherwise unfiltered OLR anomalies is constructed as follows. Unfiltered data are arranged into a new matrix \mathbf{X}^* in the same way that filtered data were arranged into the original matrix \mathbf{X} . Temporal smoothing is applied to prevent information from being lost between time

steps, and it reduces the impact of noise on the PCs. Data are smoothed by centered moving averages in time prior to placement in the matrix (except data are not smoothed if the time step between neighboring lags is 1 day). The width of the smoothing window for the data at a given time lag is equal to the timestep to the nearest neighboring window plus 1 (e.g., consider a 50-day lead—if the neighboring leads are at 42 days and 60 days, then the smoothing window is 9 days $(50-42)+1$).

(2.2.6) Generate Indices of Projections of Unfiltered Data onto the EEOF Modes

The PCs \mathbf{u} are the projections of the data matrix X^* onto the eigenvectors \mathbf{e} ($\mathbf{u}=\mathbf{X}^*\mathbf{e}$). These PCs are approximations for similar PCs that can be constructed based on the filtered data, except that these constructions can be applied in real time without distortion. The original filtered data X can be approximately reconstructed by projecting some number of the leading PCs \mathbf{u} onto the corresponding eigenvectors \mathbf{e} (e.g., $X=\mathbf{e}\mathbf{u}^T$). Small correlations are evident between reconstructed PCs \mathbf{u} based on different filter bands, so to prevent any bleeding of information from low-frequency processes onto high frequency ones, reconstructed 100-day low pass filtered OLR is subtracted before constructing the PCs for the other modes, reconstructed MJO anomalies are subtracted from the unfiltered data before calculating the PCs for the wave modes, and reconstructed ER anomalies are subtracted before calculating the PCs for the higher frequency waves. This reconstruction process approximates the result of wavenumber-frequency filtering. The process of removing the MJO prior to calculating the projections of other modes might influence the behavior of ER wave signals in the ER wave projections since some of these waves develop with the MJO (e.g., Roundy and Frank 2004b). Similarly, removal of ER waves before calculation of the 2-10 day westward waves may similarly

influence the signals of the 2-10 day waves since these might not be orthogonal to the patterns in the ER band. Since the algorithm utilizes only historical information relative to each time step, it is unaffected by the proximity of the end of the dataset, making it convenient for real time applications.

(3) Results

(3.1) Overview

The projection algorithm was applied to generate PC time series and to filter data for the wavenumber-frequency bands discussed above. The main objective of this section is to demonstrate the application of the method as a substitute for filtering in the wavenumber frequency domain. Another objective is to demonstrate the behaviors of selected time indices of modes that can be utilized in statistical models for prediction of the wave and climate patterns and their global impacts. The structures and climatologies of selected individual eigenmodes will only be considered briefly here, but will be analyzed more thoroughly in subsequent papers. For reference, the cumulative fraction variance explained by the leading 100 EEOFs of each of the five bands is shown in Fig. 2.

(3.2) Individual Cases

An example of reconstructed MJO-band OLR anomalies is given in Fig. 3. Figure 3a shows the projected signal of the MJO (contours) superimposed on unfiltered OLR anomalies (shading) averaged across 7.5°N to 7.5°S . Figure 3b shows the projected signal (shading) with wavenumber-frequency filtered data (contours). These projections include the first 25 EEOFs (this selection is arbitrary, but the structures obtained are not sensitive to small changes in the numbers of EEOFs included past EEOF 20, the number

retained can be adjusted based on the needs of the user and preferred retaining criterion such as that of North et al. (1982)). Anomalous active convection is shaded in blue. A series of alternating active and suppressed convective events is apparent in each field, propagating eastward in a manner consistent with the MJO. This result demonstrates that the projected data is well phased with anomalies in both the unfiltered and MJO-filtered OLR. The amplitudes of the filtered and projected OLR are also similar, and the temporal correlation coefficients exceed 0.7 on the equator over the warm pool regions of the Indian and West Pacific basins but are as low as 0.37 over the equatorial East Pacific, where convection is generally suppressed. The filtered data would include distortions associated with the Gibbs ringing phenomenon, which would not appear in these projections. Further, wavenumber-frequency-filtered data would include more background noise, since most of this noise would be eliminated by including only the leading PCs in the reconstruction. Since the projection method utilizes structures evolving systematically in space and time, it might actually provide a better estimate of MJO signal than the filtered data. Inclusion of data over a long time window by the method would frequently improve its representation.

An example for projected 2-10 day-westward filtered OLR is given in Fig. 4. As with the MJO band, projected and filtered OLR are generally similar and provide a reasonable match to disturbances seen in unfiltered anomalies. Projections of Kelvin-filtered OLR (not shown) are also similar to Kelvin-filtered OLR, except for a smoothing of high wavenumber structures in comparison with the filtered data.

(3.3) Spectrum Analysis

A spectrum analysis is applied to test whether the output of the EEOF-reconstructed data for each band of the wavenumber frequency domain is consistent with the targeted region of the spectrum. Wavenumber-frequency spectrum analysis was applied after the manner of Wheeler and Kiladis (1999) to data processed for each of the 4 wave bands plotted on Fig. 1. The projected data for each latitude were broken into many consecutively overlapping longitude time segments (each segment was global in longitude and 170-days long). Each segment was tapered in time by cosine bells, then a Fourier transform was taken in longitude and another in time. Spectral power was obtained by multiplying this transform by its complex conjugate. An overlap of 85 days was applied between segments (to recover data lost by the tapering). As in Wheeler and Kiladis (1999), results are not sensitive to the precise extent of this overlap. The set of the spectra of all segments were then averaged over all latitudes from 15°N to 15°S (cross-equatorial symmetry was not considered). The same analysis was also performed for unprocessed OLR anomalies in order to estimate a ‘background’ spectrum, except that the projected OLR anomalies including the first 25 PCs of each filter band were subtracted first, leaving behind the ‘noise’. Inclusion of 25 PCs might seem arbitrarily large, but the total number of PCs exceeds 11,000. We estimate that retention of 25 PCs accounts for only 15-57% of the variance, depending on the filter band (Fig 2). This removal of the wave signal from the background would arguably generate a more appropriate red noise background than could be obtained based on the total signal, since the smoothing process used to construct the background following Wheeler and Kiladis (1999) and Roundy and Frank (2004a) conserves power associated with the waves

themselves within the background. This background spectrum was smoothed 15 times in wavenumber and in frequency with a one-two-one filter, and normalized spectra for each of the four processed datasets were generated by dividing their respective spectra by this background. Figure 5 shows the results for a, the MJO, b, ER waves, c, Kelvin waves, and d, 2-10 day westward-moving waves. Filter bands are plotted on Fig. 5 for comparison with Fig. 1. Values smaller than one suggest that the projected wave patterns are associated with less variance than the background (or, in other words, that the signal strength is weak, e.g., Hendon and Wheeler 2008). Weak signal strength does not imply that the associated anomalies are insignificant or inconsequential. One benefit of this algorithm is that it extracts the part of the signal that evolves systematically in time and space while excluding most background noise. These results are consistent with the interpretation that the signal to noise ratio is highest in the MJO band followed by the Kelvin band, and lowest in the 2-10 day westward and ER bands. Determining the precise signal to noise ratio would necessarily be subjective since some method would need to be applied to determine whether a given PC represents signal or noise. North's rule of thumb (e.g., North et al. 1982) estimates only whether a given PC or group of PCs can be treated independent of its neighbors. In any case, most predictability in tropical convection would be found within these projected patterns associated with the leading PCs.

The spectra in Fig. 5 illustrate to what extent the projection process generates results consistent with the initial wavenumber-frequency filtering. Each spectrum shows that most of the power in projected data is consistent with the distribution of power in the original filter bands outlined in Fig. 1. Projections of 2-10 day westward anomalies

exhibit peak power in the same region of the spectrum as MRG waves analyzed by Wheeler and Kiladis (1999), but Fig. 4 suggests that this method is also useful for tracking African easterly waves from their origins westward across the Atlantic and over the Northeast Pacific with some zonal smoothing of the projected anomalies. The Kelvin, ER, and MJO spectra are roughly consistent with Wheeler and Kiladis (1999), with the principal exception being that power at wavenumbers greater than 10 is reduced by the projection algorithm. The Kelvin peak appears to be shifted slightly to the left of the corresponding peak in Fig. 1, suggesting the possibility that the background assumed in Fig. 1 includes too much power in that region.

(3.4) MJO Indices

(3.4.1) First two EEOFs

Since Wheeler and Hendon (2004) applied an EOF analysis of zonal winds and OLR to construct the Real-time Multivariate MJO (RMM) PCs, it is of interest to compare PCs generated based on the present technique with theirs. We averaged the first and second EEOFs of the MJO band across 15°N to 15°S at the zero day time lag, compared the results with the OLR portions of the first and second RMM EOFs, and found them to correspond well, except that the first (second) EEOF corresponds with RMM2 (RMM1). For reference, the corresponding EEOF patterns including all time lags are shown in Fig. 6. The expected pattern of eastward propagation, with the Indian and West Pacific basins alternating between active and suppressed phases is clearly evident in Fig. 6. We calculated the mean phase difference between the EEOF PCs and that of WH04, and found it to be near zero after adjusting for signs and order. Figure 7 a-c shows three randomly selected periods with both the RMM PCs and the MJO-EEOF PCs together.

Both the RMM PCs and the EEOF PCs suggest phase rotation in the counter clockwise direction, beginning and ending in roughly the same regions of the phase space. However, the EEOF MJO PCs vary more smoothly with time than do the RMM PCs. Although the MJO is the leading contributor to variance in the RMM PCs, they vary erratically in response to high frequency signals other than the MJO. Roundy et al. (2008) showed that some of these rapid variations are associated with projection of convectively coupled Kelvin waves onto the RMM EOFs. The beauty of the RMM PCs is the relative simplicity of their calculation. The first two EEOF PCs actually account for less variance in the MJO than do the RMM PCs, because WH04 reduced the degrees of freedom in their data by averaging over latitude prior to calculating the EOFs. That same variance would be explained collectively within the EEOF PCs, but would be spread among a larger number.

(3.4.2) Association of Higher EEOFs with the MJO

It is important to mention here that no 2-dimensional phase space can fully characterize the evolution of the MJO. The actual dimensionality of the MJO is unknown. Kessler (2002) demonstrated that some EOFs of equatorial zonal wind higher than the first pair describe how the MJO varies with ENSO. The higher EEOF PCs follow similar patterns, each associated with a different mode of variation of the MJO. We include here one example to illustrate. Figure 8a shows the spatial pattern of EEOFs 1 and 2 at the zero day time lag. Figure 8b shows the corresponding pattern for EEOFs 5 and 6. The predominantly symmetric cross-equatorial convective pattern associated with the MJO is contained in PC1 and PC2. EEOFs 5 and 6 are characterized by OLR anomaly patterns that are antisymmetric across the equator. Linear combinations of

EEOFs 1 and 2 with EEOFs 5 and 6 therefore diminish the total OLR anomaly on one side of the equator and enhance it on the other, allowing the combination of these patterns to represent the meridional evolution of the MJO OLR anomalies with the seasons. Examination of PCs 1 and 2 with PCs 5 and 6 reveals that they are correlated part of the year and anticorrelated the opposite part of the year. For example, PC1 is correlated at -0.47 with PC5 during December through February, and at +0.59 during June through August for the period 1974-2006. Figure 8c shows the sum of PCs 1 and 2 with PCs 5 and 6, giving the pattern of the MJO during the northern hemisphere warm season. Figure 8d shows PCs 1 and 2 minus PCs 5 and 6, and the result is consistent with the MJO anomaly patterns observed during December through February.

(3.5) Projected PCs Linked to ENSO

By projecting OLR anomalies onto the EEOFs of 100-day low pass filtered OLR, we obtain PCs for a variety of climate modes. The first of these is plotted in black in Fig. 9, and the second is plotted in gray. Local maxima in PC 2 correspond with El Niño events and are generally consistent with the timing of these events observed in Niño 3.4 SST data (plotted in the dashed curve). PC2 is in temporal quadrature with PC1. When considered with the corresponding EEOF temporal and spatial pattern (not shown), the two modes together represent a standing and eastward-propagating pattern of global convection associated with ENSO. This result suggests that the stage of ENSO can be characterized by amplitude and an angle in a phase space (although Penland and Sardeshmukh 1995 suggest that a full characterization of the state of ENSO requires at least 6-8 dimensions). Figure 10 shows the phase space generated from the first two PCs over the length of the dataset. Wide loops extending through the right two quadrants and

the upper left quadrant represent El Niño events. The PCs spend more time in quadrant 1 than any other quadrant. If this phase space provides a good partial representation of ENSO variation (neglecting relevant higher EEOFs), then it implies that categorizing the state of ENSO as El Niño, La Niña, or neutral would constitute an oversimplification of a continuously varying ENSO state. For example, it would be possible for ENSO to be in neutral conditions and be characterized by high amplitude in atmospheric convection at the same time. Such a state might exhibit anomalously active moist deep convection in regions where convection tends to be most active in the climatological mean (e.g., over the tropical West Pacific). Since this article is intended to give only a general overview of the results of the projection algorithm, further analysis of the PCs tied to ENSO will be included in a future article. Higher order PCs of the low-pass filtered OLR anomalies are associated with other processes, including the portion of the Indian Ocean dipole that is not correlated with ENSO (not shown).

(4) Conclusions

An algorithm applicable for real time diagnosis and tracking of signals of moist deep convection associated with the MJO, convectively coupled equatorial waves, ENSO, and other modes successfully isolates signals associated with the target modes. Filtered data reconstructed by the method compare well with data filtered for the same target bands in the wavenumber-frequency domain, but would not include signals associated with Gibbs ringing and would exhibit reduced noise in comparison with filtered data. Since only historical data are utilized to generate the PCs at a given time, the ends of the dataset would not be distorted by the algorithm as would data filtered in the wavenumber frequency domain. Spectra estimated for these reconstructed data agree

well with the spectra of Wheeler and Kiladis (1999) and Roundy and Frank (2004) within the respective filter bands.

The PCs obtained for the MJO by this approach are generally consistent with, but more smoothly varying than, the similar PCs developed by the combined EOF analysis of OLR and zonal wind anomalies of Wheeler and Hendon (2004). The leading pair of EEOF PCs explain less variance than the RMM PCs, because variance in the EEOF PCs is distributed over a larger basis. This broader distribution of variance is a consequence of inclusion of the additional dimensions of time and latitude (Wheeler and Hendon 2004 averaged OLR and wind data over 15°N to 15°S before calculating the leading modes), even accounting for the inclusion of zonal wind data by Wheeler and Hendon (2004). Utilization of additional modes higher than the first two help to specify the zonal and meridional structures of specific MJO events.

A pair of PCs based on 100-day low pass filtered OLR describes a standing and eastward-moving mode of atmospheric convection associated with ENSO. These two PCs can be applied together to define an ENSO phase diagram in which ENSO is described by both an amplitude and a phase angle. Additional PCs would be required to more fully characterize ENSO (e.g., Penland and Sardeshmukh 1995).

Further sets of PCs are obtained for convectively coupled Kelvin waves, equatorial Rossby waves, and 2-10 day westward moving waves. The EEOF PCs may prove useful in statistical models for weather prediction.

Acknowledgements: Funding was provided by a start-up account for new faculty provided to Dr. Roundy by the University at Albany. Discussions with George Kiladis and Matthew Wheeler were useful in developing the projection algorithm.

Works Cited

- Bessafi M, Wheeler MC. 2006. Modulation of South Indian Ocean tropical cyclones by the Madden-Julian Oscillation and convectively coupled equatorial waves. *Mon. Wea. Rev.* **134**: 638-656.
- Carlson TN. 1969. Synoptic histories of three African disturbances that developed into Atlantic Hurricanes. *Mon. Wea. Rev.* **97**: 256-276.
- Frank WM, PE Roundy. 2006. The role of tropical waves in tropical cyclogenesis. *Mon. Wea. Rev.* **113**: 647-658.
- Gruber A. 1974. The wavenumber-frequency spectra of satellite-measured brightness in the tropics. *J. Atmos. Sci.* **31**: 1675-1680.
- Hendon HH, Wheeler MC. 2008. Some space-time spectral analyses of tropical convection and planetary-scale waves. *J. Atmos. Sci.*, *submitted*.
- Hoskins BJ, Yang G-Y. 2000. The equatorial response to higher latitude forcing. *J. Atmos. Sci.* **57**: 1197-1213.
- Kessler WS. 2001. EOF representations of the Madden-Julian Oscillation and its connection with ENSO. *J. Climate* **14**: 3055-3061.
- Kiladis GN, Thorncroft CD, Hall NMJ. 2006. Three dimensional structure and dynamics of African easterly waves. Part I: Observations. *J. Atmos. Sci.* **63**: 2212-2230.
- Kiladis GN, Wheeler MC, Haertel PT, Straub KH, Roundy PE. 2000. Convectively coupled equatorial waves. *Rev. of Geophys.*, Accepted.
- Liebmann B, and Hendon HH. 1990. Synoptic-scale disturbances near the equator. *J. Atmos. Sci.* **47**: 1463-1479.
- Liebmann B, Smith CA. 1996. Description of a complete (interpolated) OLR dataset.

- Bull. Amer. Meteor. Soc.* **77**: 1275 -1277.
- Lin J-L, Weickmann KM, Kiladis GN, Mapes BE, Sperber KR, Lin W, Wheeler MC, Schubert SD, Genio AD, Donner LJ, Emori S, Gueremy J-F, Hourdin F, Rasch PJ, Roeckner E, Scinocco JF. 2006. Tropical intraseasonal variability in 14 IPCC AR4 Climate Models. Part I: Convective signals. *J. Climate* **19**: 2665-2690.
- Lindzen RS, 1967. Planetary waves on beta-planes. *Mon. Wea. Rev.* **95**: 441-451.
- Lindzen RS. 1971. Equatorial planetary-scale waves in shear: Part I. *J. Atmos. Sci.* **28**: 609-622.
- Lindzen RS. 2003. The interaction of waves and convection in the tropics. *J. Atmos. Sci.* **60**: 3009-3020.
- Madden R, and Julian P. 1994. Observations of the 40-50-day tropical oscillation- A review. *Mon. Wea. Rev.* **122**: 814-837.
- Majda AJ, Khouider B, Kiladis GN, Straub KH, Shefter MG. 2004. A model for convectively coupled tropical waves: Nonlinearity, rotation, and comparison with observations. *J. Atmos. Sci.* **61**: 2188-2205.
- Matsuno T. 1966. Quasi-geostrophic motions in the equatorial area. *J. Meteor. Soc. Japan* **44**: 25-43.
- North GR, Bell TL, Cahalan RF, Moenig FJ. 1982. Sampling errors in the estimation of empirical orthogonal functions. *Mon. Wea. Rev.* **110**: 669-706.
- Reed RJ, Norquist DC, and Recker EE. 1977. The structure and properties of African wave disturbances as observed during Phase III of GATE. *Mon. Wea. Rev.* **105**: 317-333.

- Penland C, Sardeshmukh PD. 1995. The optimal growth of tropical sea surface temperature anomalies, *J. Climate*, **8**: 1999-2024.
- Roundy PE, 2008: Analysis of convectively coupled Kelvin waves in the Indian Ocean MJO. *J. Atmos. Sci.* **65**: 1342-1359.
- Roundy PE, Frank WM. 2004a. A climatology of waves in the equatorial region. *J. Atmos. Sci.* **61**: 2105-2132.
- Roundy PE, and Frank WM. 2004b. Effects of low-frequency wave interactions on intraseasonal oscillations. *J. Atmos. Sci.* **61**: 3025-3040.
- Takayabu YN. 1994. Large-scale cloud disturbances associated with equatorial waves. Part I: Spectral features of the cloud disturbances. *J. Meteor. Soc. Japan* **72**: 433-448.
- Waliser DE, Jones C, Schemm J-K, Graham NE. 1999. A statistical extended-range tropical forecast model based on the slow evolution of the Madden-Julian Oscillation. *J. Climate* **12**: 1918-1939.
- Wallace JM, Chang LA. 1972. On the application of satellite data on the cloud brightness to the study of tropical wave disturbances. *J. Atmos. Sci.* **29**: 1400-1403.
- Wang B, Xie X. 1996. Low-frequency equatorial waves in vertically sheared zonal flow. Part I: Stable waves. *J. Atmos. Sci.* **53**: 449-467.
- Weare BC. 2003. Composite singular value decomposition analysis of moisture variations associated with the Madden-Julian Oscillation. *J. Climate* **16**: 3779-3792.
- Weickmann KM, Lussy GR, Kutzbach JE. 1985. Intraseasonal (30-60 day) fluctuations of outgoing longwave radiation and 250 mb streamfunction during northern

- winter. *Mon. Wea. Rev.* **113**: 941-961.
- Weickmann KM, Kiladis GN, Sardeshmukh PD. 1997. The dynamics of intraseasonal atmospheric angular momentum oscillations. *J. Atmos. Sci.* **54**: 1445-1461.
- Wheeler MC, Hendon HH. 2004. An all-season real-time multivariate MJO index: Development of an index for monitoring and prediction. *Mon. Wea. Rev.* **132**: 1917-1932.
- Wheeler M, and Kiladis GN. 1999. Convectively-coupled equatorial waves: Analysis of clouds in the wavenumber-frequency domain. *J. Atmos. Sci.* **56**: 374-399.
- Wheeler M, Kiladis GN, Webster PJ. 2000. Large-scale dynamical fields associated with convectively-coupled equatorial waves. *J. Atmos. Sci.* **57**: 613-640.
- Wheeler MC, and Weickmann KM. 2001. Real time monitoring and prediction of modes of coherent synoptic to intraseasonal tropical variability. *Mon. Wea. Rev.* **129**: 2677-2694.
- Yanai, M, Murakami M. 1970. Spectrum analysis of symmetric and anti-symmetric equatorial waves. *J. Meteor. Soc. Japan* **48**: 331-347.
- Yang G -Y, Hoskins B, and Slingo J. 2003. Convectively coupled equatorial waves: A new methodology for identifying wave structures in observational data. *J. Atmos. Sci.* **60**: 1637-1654.
- Yang G-Y, Hoskins B, and Slingo J. 2007a. Convectively coupled equatorial waves. Part I: Horizontal and vertical structures. *J. Atmos. Sci.* **64**: 3406-3423.
- Yang G-Y, Hoskins B, Slingo J. 2007b. Convectively coupled equatorial waves. Part II: Propagation characteristics. *J. Atmos. Sci.* **64**: 3424-3437.
- Yang G-Y, Hoskins B, Slingo J. 2007c. Convectively coupled equatorial waves. Part III:

- Synthesis structures and their forcing and evolution. *J. Atmos. Sci.* **64**: 3438-3451.
- Zangvil A. 1975. Temporal and spatial behavior of large-scale disturbances in tropical cloudiness deduced from satellite brightness data. *Mon. Wea. Rev.* **103**: 904-920.
- Zangvil A, Yanai M. 1980. Upper tropospheric waves in the tropics. Part I: Dynamical analysis in the wavenumber-frequency domain. *J. Atmos. Sci.* **37**: 283-298.
- Zangvil A, Yanai M. 1981. Upper tropospheric waves in the tropics. Part II: Association with clouds in the wavenumber-frequency domain. *J. Atmos. Sci.* **38**: 939-953.
- Zhang, C. 2005. The Madden-Julian Oscillation. *Rev. Geophys.* **43**: RG2003, doi:10.1029/2004RG000158.
- Zhang C, Hendon HH. 1997. Propagating and stationary components of the intraseasonal oscillation in tropical convection. *J. Atmos. Sci.* **54**: 741-752.

List of Tables

Table I: Time lags associated with the 13 temporal extensions of each data matrices according to target filter band.

List of Figures

Figure 1: Bands of the wavenumber frequency domain utilized as filters to concentrate signals associated with the 4 primary types of waves and intraseasonal oscillations discussed in the text, plotted on a spectrum of OLR anomalies calculated at each latitude and averaged over 15°N to 15°S and divided by an estimated red background.

Figure 2: Cumulative fraction of the total variance explained by retaining up to the n th leading principal component for ER waves, the MJO, Kelvin waves, 2-10 day westward-moving waves, and 100-day low pass patterns.

Figure 3: a. Unfiltered OLR anomalies (shaded), with contours of EEOF reconstructed OLR anomalies for the MJO. Negative MJO OLR anomalies are contoured red, and positive are blue. The contour interval is 7.5 Wm^{-2} , with the lowest contours at $\pm 5 \text{ Wm}^{-2}$. b. EEOF reconstructed OLR for the MJO plotted as in (a), with OLR filtered in the wavenumber frequency domain for the MJO shaded.

Figure 4: Same as Figure 2, except for 2-10 day westward-filtered OLR. The contour interval for the projected OLR anomalies is 7.5 Wm^{-2} , with the lowest contours at $\pm 2 \text{ Wm}^{-2}$.

Figure 5: Spectra of (a), MJO, (b) ER wave, (c) Kelvin wave, and (d) 2-10 day westward-moving waves estimated by the EEOF projection method discussed in the text, averaged over 15°N to 15°S. Spectra are normalized by dividing by a red background, estimated as discussed in the text. Boxes outline the same filter bands shown in Fig. 1.

Figure 6: Patterns of the first two EEOFs of the MJO, averaged across 15°N to 15°S.

Shading represents the first EEOF, and contours represent the second. Amplitudes are not specified because they can be scaled by multiplication by a scalar.

Figure 7: Phase portraits of the first two PCs of MJO EEOF projected OLR anomalies (gray curves) with the corresponding RMM PCs of Wheeler and Hendon (2004) (black curves). Signals rotate counter clockwise with time. The circle near the centers of the diagrams is the 1 SD level of phase amplitude. Each panel represents 50 days of observations, beginning on (a) 13 April 1987, (b) 3-December, 1988, and (c) 3 June, 2002.

Figure 8: a. Pattern of the first EEOF of the MJO band at the shortest lead-time shown in Table I (shading). The corresponding pattern of the second EEOF is shown in contours. b. Pattern of the fifth EEOF (shading) and sixth EEOF (contours) at the same lead-time as shown in Panel a. c. The sum of (a) and (b). d. (a) minus (b).

Figure 9: The first PC of 100-day lowpass projected OLR anomalies (solid black curve). The second PC is plotted in solid gray. Monthly mean Niño 3.4 SST anomalies are plotted for reference in the dashed gray curve. All values are normalized by dividing by the respective standard deviations.

Figure 10: The phase space generated by plotting the first two PCs of low pass filtered OLR shown in Fig. 9. Superimposed numbers represent the last two digits of the year, and they indicate January 1.

Table I: Time Lags (in Days) for EEOF Matrix Extensions					
Step Number	100-day Lowpass	MJO	ER	Kelvin	2-10 day westward
1	11	3	3	1	1
2	30	7	7	2	2
3	49	12	12	3	3
4	68	17	17	4	4
5	89	22	22	5	5
6	116	27	27	6	6
7	147	32	32	7	7
8	178	39	38	8	8
9	209	48	46	10	9
10	240	58	55	13	10
11	271	69	65	16	11
12	318	81	76	19	12
13	381	94	88	23	13

Table I: Number of days prior to day 0 for each matrix extension according to the different target modes.

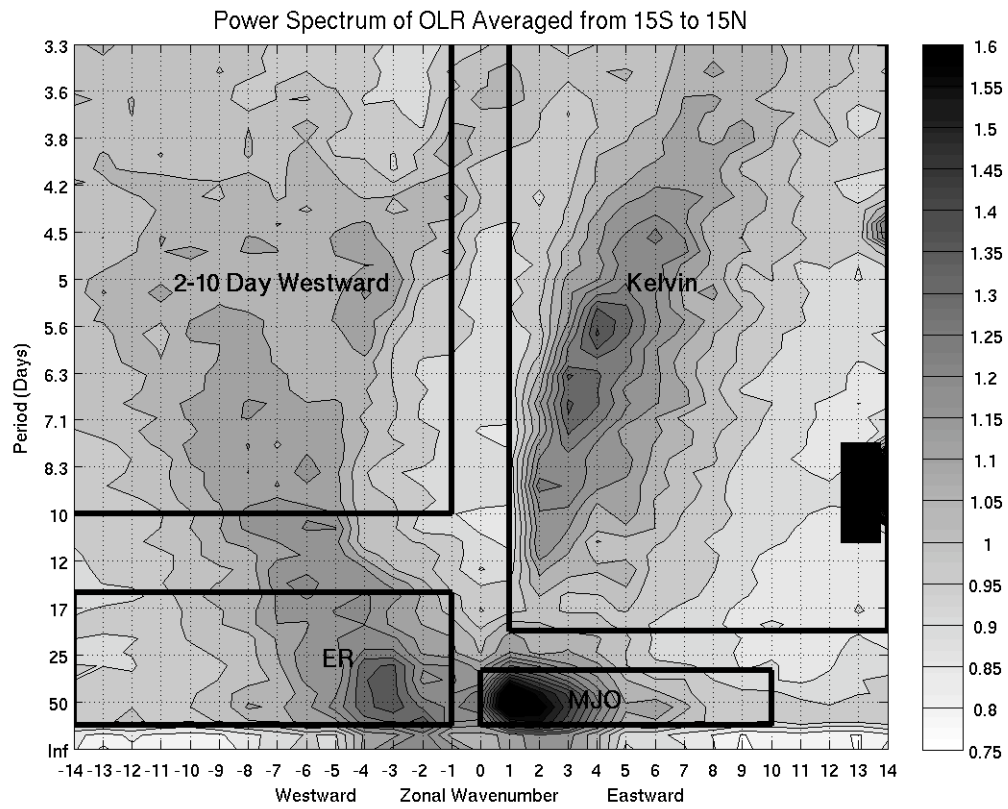


Figure 1: Bands of the wavenumber frequency domain utilized as filters to concentrate signals associated with the 4 primary types of waves and intraseasonal oscillations discussed in the text, plotted on a spectrum of OLR anomalies calculated at each latitude and averaged over 15°N to 15°S and divided by an estimated red background.

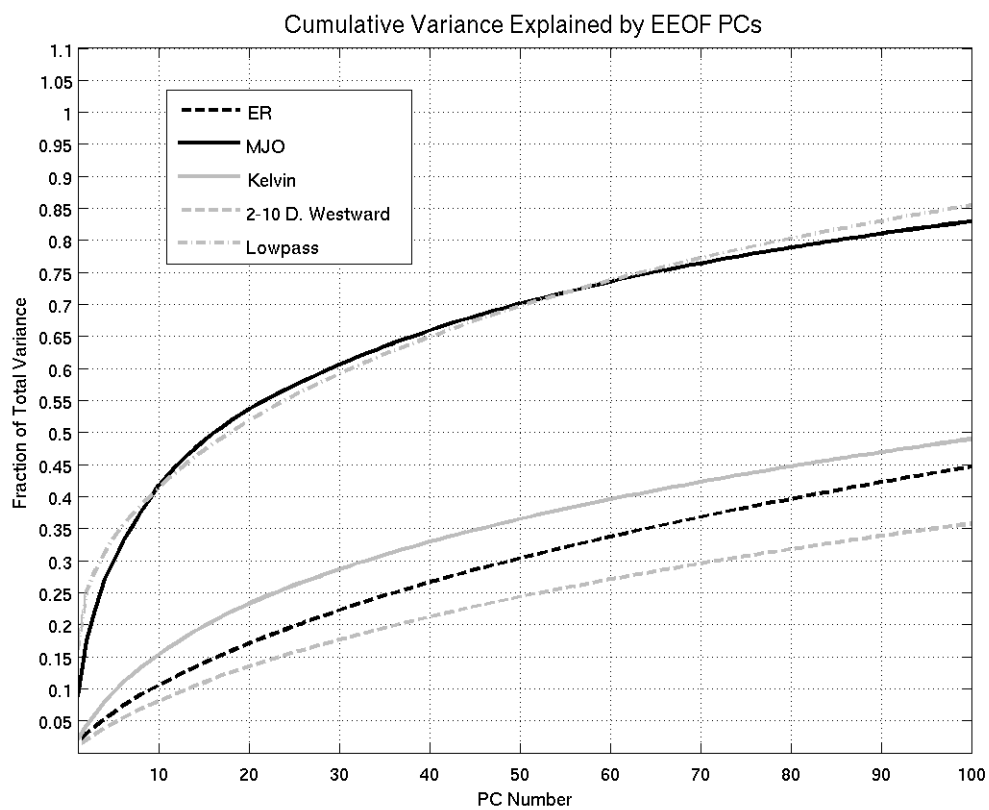


Figure 2: Cumulative fraction of the total variance explained by retaining up to the n th leading principal component for ER waves, the MJO, Kelvin waves, 2-10 day westward-moving waves, and 100-day low pass patterns.

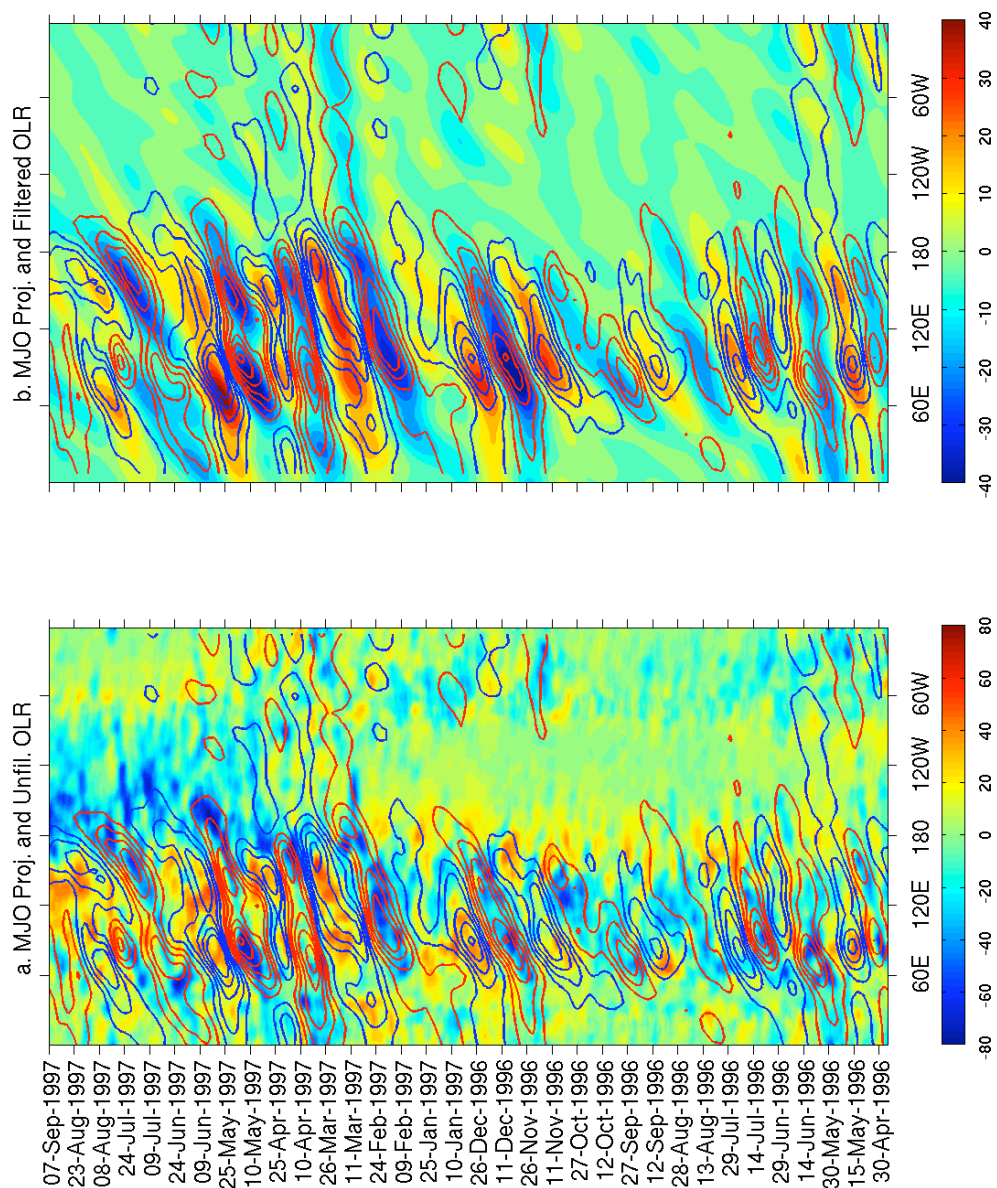


Figure 3: a. Unfiltered OLR anomalies (shaded), with contours of EEOF reconstructed OLR anomalies for the MJO. Negative MJO OLR anomalies are contoured red, and positive are blue. The contour interval is 7.5 Wm^{-2} , with the lowest contours at $\pm 5 \text{ Wm}^{-2}$. b. EEOF reconstructed OLR for the MJO plotted as in (a), with OLR filtered in the wavenumber frequency domain for the MJO shaded.

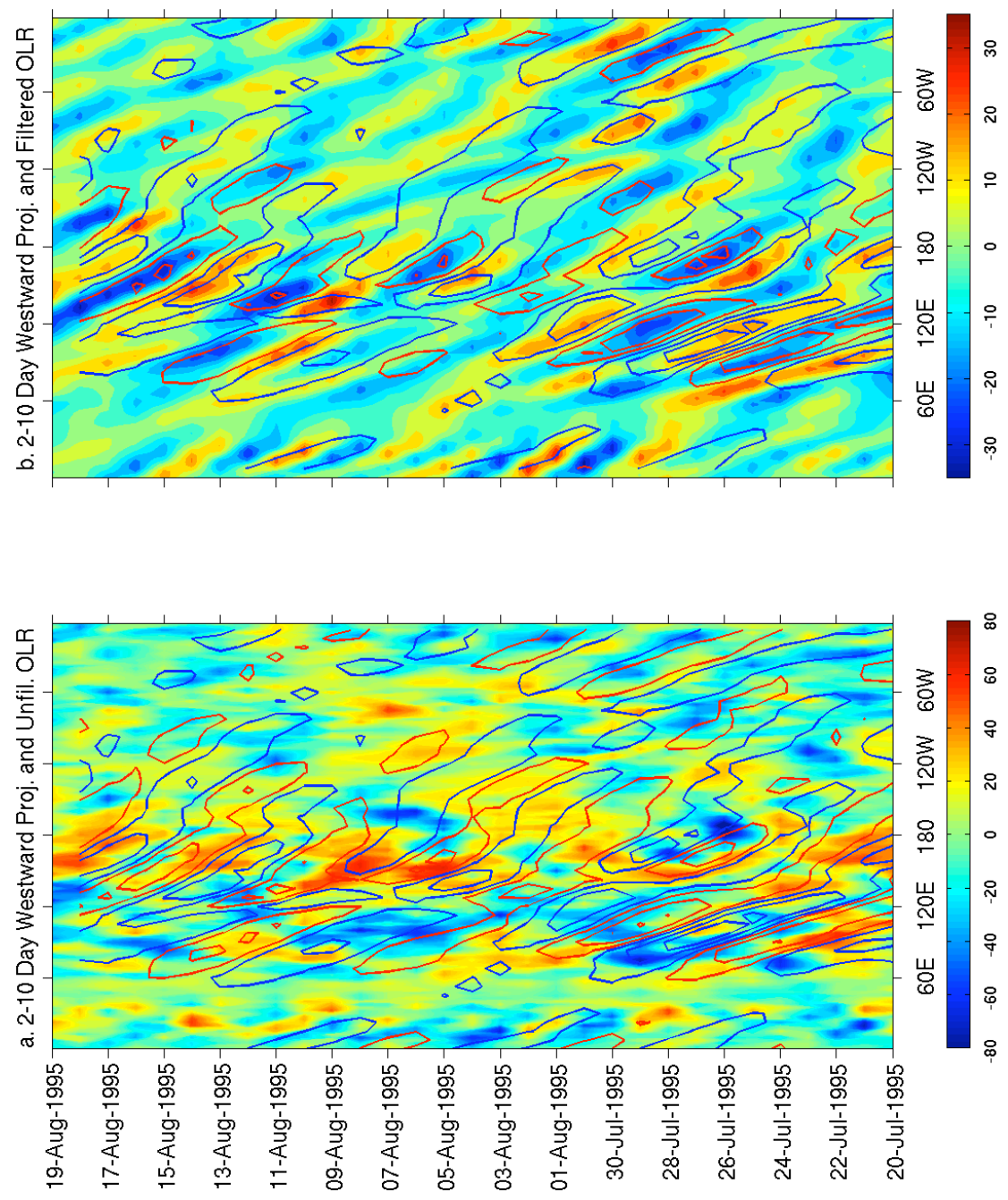


Figure 4: Same as Figure 3, except for 2-10 day westward-filtered OLR. The contour interval for the projected OLR anomalies is $7.5 Wm^{-2}$, with the lowest contours at $\pm 2 Wm^{-2}$.

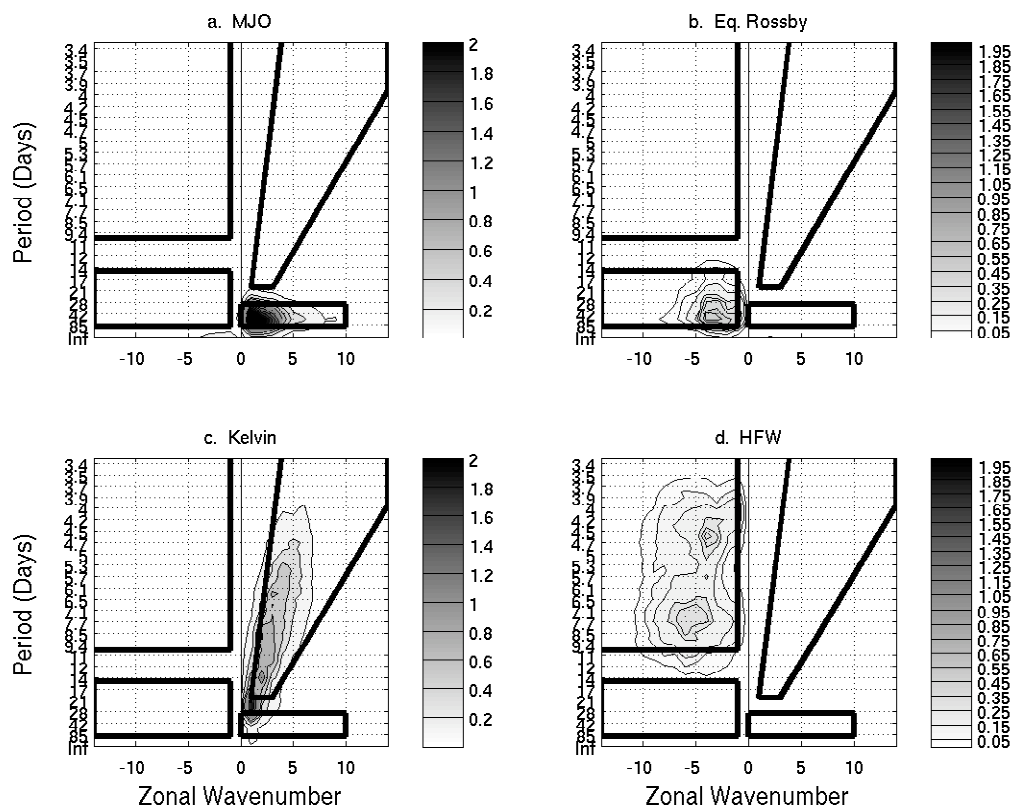


Figure 5: Spectra of (a), MJO, (b) ER wave, (c) Kelvin wave, and (d) 2-10 day westward-moving waves estimated by the EEOF projection method discussed in the text, averaged over 15°N to 15°S . Spectra are normalized by dividing by a red background, estimated as discussed in the text. Boxes outline the same filter bands shown in Fig. 1.

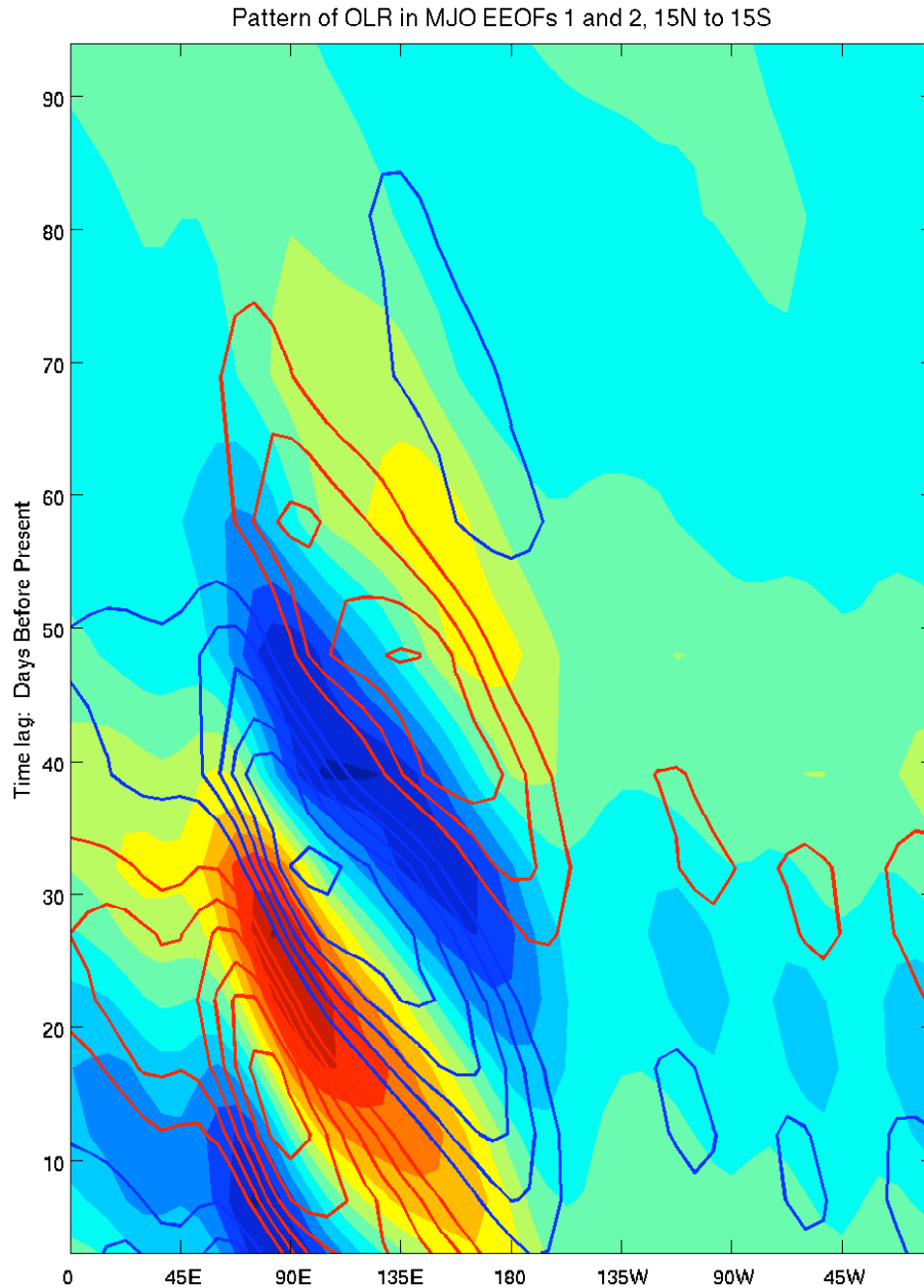


Figure 6: Patterns of the first two EEOFs of the MJO, averaged across 15°N to 15°S. Shading represents the first EEOF, and contours represent the second. Amplitudes are not specified because they can be scaled by multiplication by a scalar.

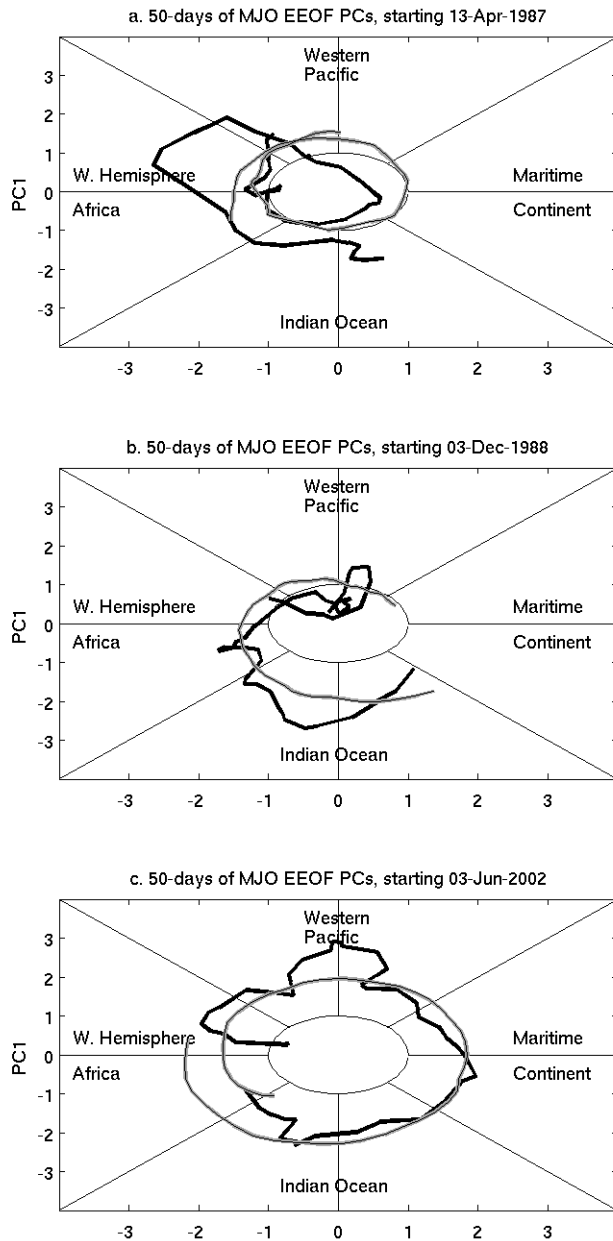


Figure 7: Phase portraits of the first two PCs of MJO EEOF projected OLR anomalies (gray curves) with the corresponding RMM PCs of Wheeler and Hendon (2004) (black curves). Signals rotate counter clockwise with time. The circle near the centers of the diagrams is the 1 SD level of phase amplitude. Each panel represents 50 days of observations, beginning on (a) 13 April 1987, (b) 3-December, 1988, and (c) 3 June, 2002.

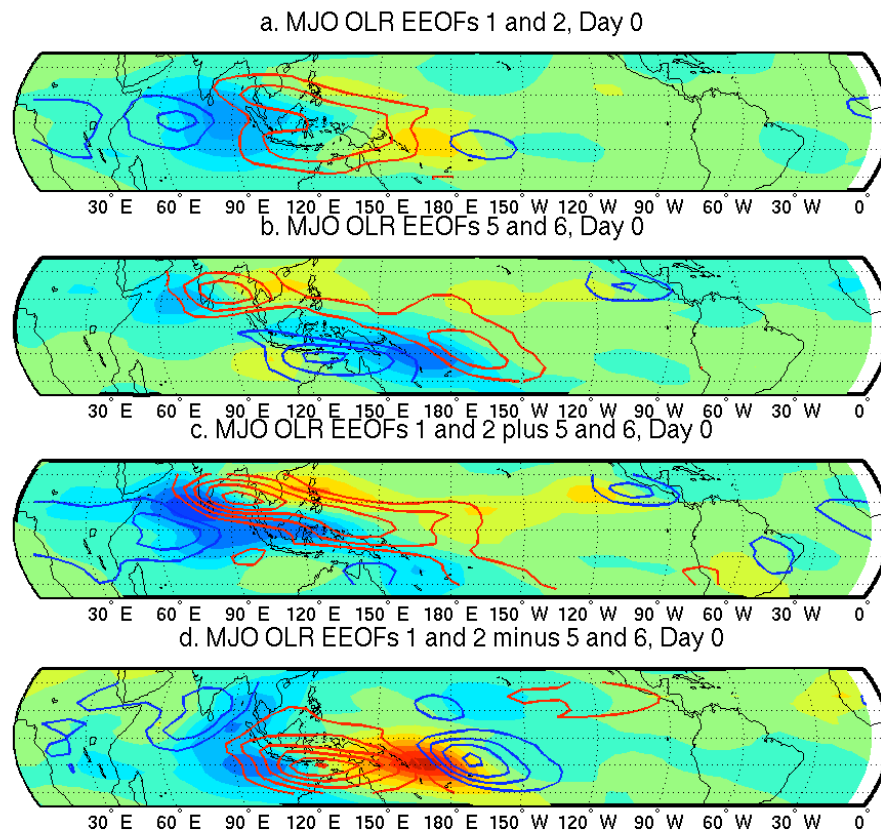


Figure 8: a. Pattern of the first EEOF of the MJO band at the shortest lead-time shown in Table I (shading). The corresponding pattern of the second EEOF is shown in contours. b. Pattern of the fifth EEOF (shading) and sixth EEOF (contours) at the same lead-time as shown in Panel a. c. The sum of (a) and (b). d. (a) minus (b).

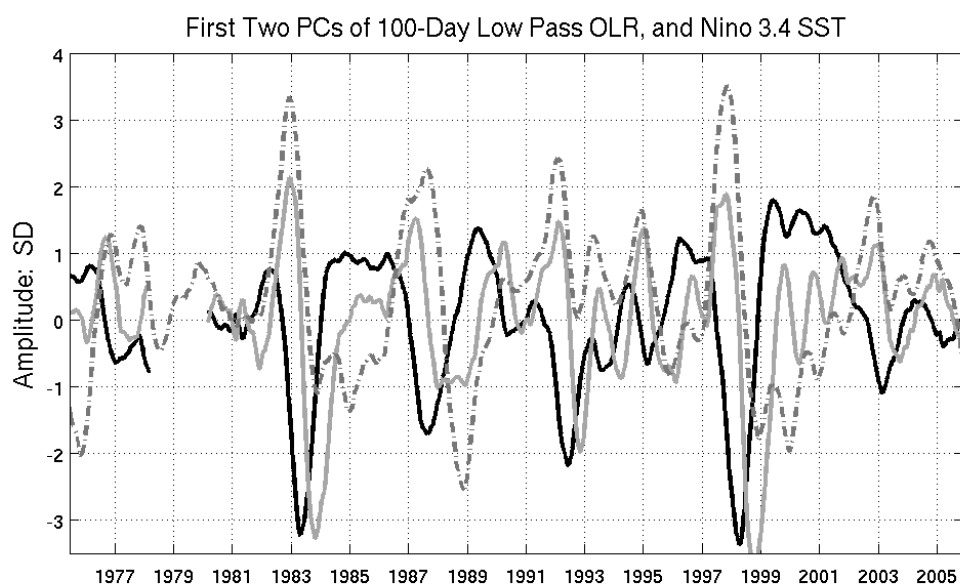


Figure 9: The first PC of 100-day lowpass projected OLR anomalies (solid black curve). The second PC is plotted in solid gray. Monthly mean Niño 3.4 SST anomalies are plotted for reference in the dashed gray curve. All values are normalized by dividing by the respective standard deviations.

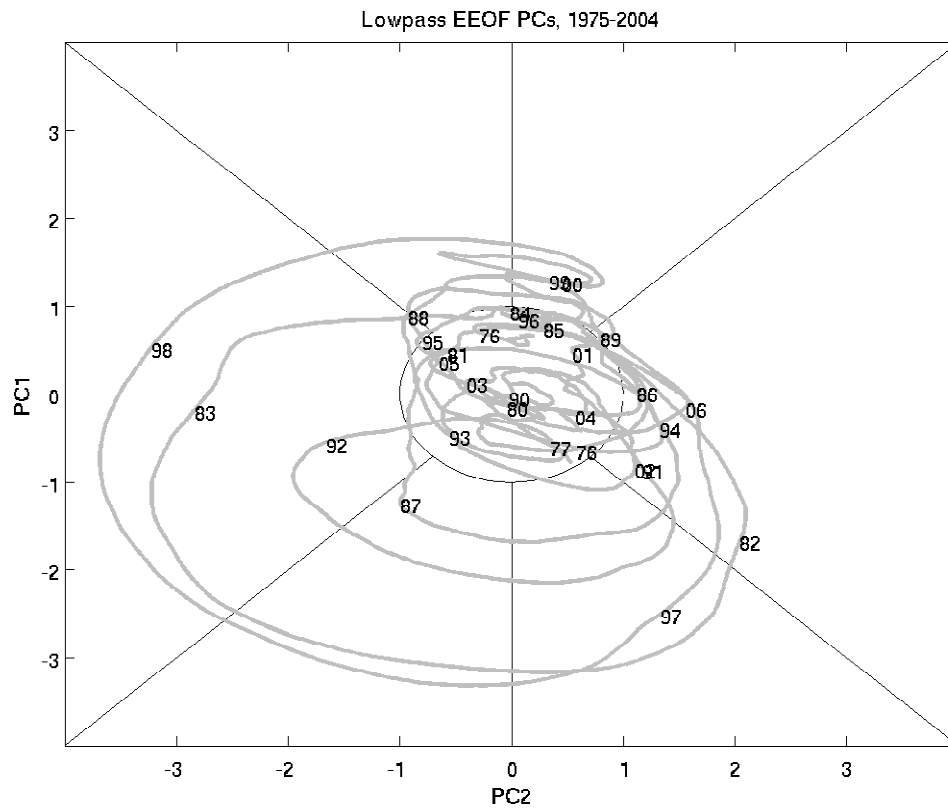


Figure 10: The phase space generated by plotting the first two PCs of low pass filtered OLR shown in Fig. 8. Superimposed numbers represent the last two digits of the year, and they indicate January 1.